# Highly-Sensitive Skin-Attachable Eye-Movement Sensor Using Flexible Nonhazardous Piezoelectric Thin Film

*Nam-In Kim, Jie Chen, Weijie Wang, Mina Moradnia, Sara Pouladi, Min-Ki Kwon, Ja-Yeon Kim, Xiaohang Li, and Jae-Hyun Ryou\**

Accurate and continuous monitoring of eye movements using compact, low-power-consuming, and easily-wearable sensors is necessary in personal and public health and safety, selected medical diagnosis techniques (point-of-care diagnostics), and personal entertainment systems. In this study, a highly sensitive, noninvasive, and skin-attachable sensor made of a stable flexible piezoelectric thin film that is also free of hazardous elements to overcome the limitations of current computer-vision-based eye-tracking systems and piezoelectric strain sensors is developed. The sensor fabricated from single-crystalline III-N thin film by a layer-transfer technique is highly sensitive and can detect subtle movements of the eye. The flexible eye movement sensor converts the mechanical deformation (skin deflection by eye blinking and eyeball motion) with various frequencies and levels into electrical outputs. The sensor can detect abnormal eye flickering and conditions caused by fatigue and drowsiness, including overlong closure, hasty eye blinking, and half-closed eyes. The abnormal eyeball motions, which may be the sign of several brain-related diseases, can also be measured, as the sensor generates discernable output voltages from the direction of eyeball movements. This study provides a practical solution for continuous sensing of human eye blinking and eyeball motion as a critical part of personal healthcare, safety, and entertainment systems.

## 1. Introduction

Besides their well-known function of providing visual information of the outside world by detecting different lights and producing images, human eyes provide the physiological information of bodies to the outside world. First, eye fatigue (or eye strain), which is commonly experienced when reading or writing and driving for an extended period, is identified as an important ocular health and safety problem,[1] especially these days as the daily use of personal electronic devices, such as laptop/desktop computers, smartphones, tablets, and gaming consoles, just to list a few, drastically increases. Among many symptoms of eye fatigue, dry eyes are the most typical symptom. One with eye fatigue frequently blinks their eyes to alleviate the symptom, which can be detected by eye movement. Second, drowsiness and fatigue, caused by sleep deprivation, tiredness, circadian rhythm effect, and temporary brain circulation problem, is a serious public safety hazard related to motor vehicle and occupational accidents. For instance, a study estimated that 7.0% of all crashes and 16.5% of fatal crashes involved a drowsy driver,[2] suggesting that more than 6000 people die in drowsy driving-related motor vehicle crashes across the United States each year,[3] which is not surprising since more than 60% of vehicle drivers have experienced drowsiness while driving.[4] Drowsiness and fatigue involve the changes in physiological parameters,[5] which allow objective and direct ways to measure them. However, their detection for the vehicle drivers and workers in field conditions is difficult due to either the intrusive and cumbersome procedures of the measurement

N.-I. Kim, Dr. J. Chen, Dr. W. Wang, M. Moradnia, Prof. J.-H. Ryou
Department of Mechanical Engineering
University of Houston
Houston, TX 77204-2004, USA
E-mail: jryou@uh.edu

N.-I. Kim, Dr. J. Chen, Dr. S. Pouladi, Prof. J.-H. Ryou
Materials Science and Engineering Program
University of Houston
Houston, TX 77204, USA

N.-I. Kim, Dr. J. Chen, Dr. W. Wang, M. Moradnia, Dr. S. Pouladi, Prof. J.-H. Ryou
Advanced Manufacturing Institute (AMI)
University of Houston
Houston, TX 77204, USA

N.-I. Kim, Dr. J. Chen, Dr. W. Wang, M. Moradnia, Dr. S. Pouladi, Prof. J.-H. Ryou
Texas Center for Superconductivity at UH (TcSUH)
University of Houston
Houston, TX 77204, USA

Prof. M.-K. Kwon
Department of Photonic Engineering
Chosun University
Gwangju 61452, Republic of Korea

Dr. J.-Y. Kim
Korea Photonics Technology Institute (KOPTI)
Gwangju 61007, Republic of Korea

Prof. X. Li
Advanced Semiconductor Laboratory
King Abdullah University of Science and Technology (KAUST)
Thuwal 23955, Saudi Arabia

(such as in electroencephalography) or the inaccuracy of the parameter as an indicator (such as the heart rate variability where the physiological features also vary with other states including emotion, workload, and physical fatigue).[6] Instead, a direct measurement of the ocular movement is a promising objective indicator of drowsiness.[7] Third, the condition of the eyes can reflect the condition of the brain, since the human eyes are one of the most connected organs to the brain through nerves and muscles. This provides a simple yet efficient way to diagnose the status of the brain.[8] Abnormal eye blinking and eyeball motion are associated with brain-related diseases, such as attention deficit hyperactivity disorder (ADHD), stroke, autism, Alzheimer's, and Parkinson's disease.[9] ADHD with tic disorder is accompanied by different types of oculomotor motions.[10] For instance, fairly sluggish saccades were observed in some of the subjects due to their hyperactivity disorder.[11] Eye-related motions are also an indicator of the imminence of a stroke.[12] Additionally, children and teenagers with autism show difficulty with the saccade test, which includes a very slow reaction.[13] Abnormalities in eye movement and eyeball motion can be detected and analyzed as one of the indicators of such diseases. Fourth, ocular movements are associated with two types of sleep pattern, nonrapid eye movement (NREM) sleep and rapid eye movement (REM) sleep,[14] which are closely connected with brain development. Especially in childhood and adolescence periods, REM sleep influences their brain development via synaptogenesis, synaptic rearrangement, and cortex synapse plasticity.[14] A significant lack of REM sleep hinders sufficient brain growth, which increases the likelihood of many of the aforementioned diseases. The tracking of eyeball motion allows us to indirectly diagnose the brain conditions and prevent brain-related diseases because the eyes are connected to the brain through many channels.[15] Fifth, eye-motion tracking becomes more important as a core technology in virtual reality (VR) and augmented reality (AR) systems. With an improved eye-tracking system (ETS) with high accuracy and fast response time, VR/AR systems can provide their users with more realistic contents while decreasing uneasiness or nausea uneasy feeling by mitigating the vergence-accommodation conflict problem in head-mounted displays.[16] In summary, the accurate and continuous monitoring of eye movement by sensitive, low-power-consuming, and compact sensors can be implemented in diverse applications of personal entertainment, public safety, and medical diagnosis.

Currently developed ETSs for ocular motions and eye blinking rely on a computer-vision-based system in various platforms of desktop-mounted, head-mounted, and in-vehicle systems. The systems require expensive and bulky components, including a high-resolution camera, mounting units (e.g., helmet, headgear, or goggle for the case of head mount), optical sensors, and an image processing software, which make their miniaturization challenging. Also, many of these camera-based systems require frequent calibration procedures for each subject or user for precise tracking.[17] In automotive systems, for example, eye tracking can be conducted using the camera installed on a dashboard or sun-visor. Under actual driving conditions, driver's motions such as head swing or nodding hinder accurate tracking of eye locations, which requires additional in-cabin 3D image sensors. This poses a greater challenge in

the problem that is even more serious for moving individuals at work or while walking. Thus, compact and easily wearable alternative ETS is demanded necessary.

Another technique to measure the eyeball movement is electrooculogram (EOG). The EOG signal comes from the potential difference between the cornea and retina. For the measurement of the potentials, the EOG system requires simultaneous measurements from several electrodes on the face (e.g., around eyelid and temple) and neck. The output signal from the EOG is relatively weak (less than several mV) and is easily influenced by the experimental conditions. Therefore, the application of EOG as a versatile eye movement sensor has been limited except for the selected eye-function-related medical diagnosis.

Flexible epidermic sensors can provide a solution to overcome the drawbacks of current ETS. Specifically, skin-attachable piezoelectric eye-movement sensors (PEMS) inherently have advantages in size, weight, power, and cost (SWaP-C). They are compact (the order of mm in dimension), light-weight (less than a gram), and self-powered (no power supply required for the operation of the sensor). Besides the SWaP advantages, their bendability and conformal nature with a significantly reduced thickness (≈1 mm or less) allow the flexible PEMS (F-PEMS) to be skin-attachable without causing discomfort, i.e., easily wearable and noninvasive. The skin-attachable sensors also result in improved sensing capability without calibration while not sacrificing sensitivity and response time. The sensing system including sensors and wireless communication circuits is significantly cheaper and lower power consumption than the video-based ETS. With the advantages, F-PEMS can offer a great opportunity in personal healthcare and safety monitoring, additional medical diagnosis, and AR/VR systems.

In the previous studies, strain sensors have been used to indirectly detect the movement of eyes by attaching them directly on the eyelid. The piezoelectric strain sensors based on lead zirconate titanate ($Pb[Zr_xTi_{1-x}]O_3$, PZT) and zinc oxide (ZnO) were able to measure the strain change on the eyelids upon their moving;[18] however, they showed limitations as a wearable and reliable sensor. PZT contains a significant amount of harmful lead, which causes poisoning in the human body. Wearable and implantable sensors should be toxic-element-free by all means. ZnO sensor showed low sensitivity and resolution,[18a,d] which requires additional signal processing of amplification and noise reduction. The benefit of no toxicity of ZnO cannot compensate for low sensing performance, the most fundamental function of the sensors. Most importantly, all the previous sensors were attached directly on the eyelid where the most sensitive output signals from the surface strain change can be obtained at the expense of comfort and safety. The previous sensors are not truly noninvasive for safe and comfortable wearing.

Alternative piezoelectric sensing elements have been sought for in healthcare monitoring systems to replace safety-hazard-ridden PZT while achieving high electromechanical coupling factors comparable to PZT. Single-crystalline group III-N materials, especially gallium nitride (GaN) thin films, have been recently proposed for an excellent piezoelectric sensing and energy-harvesting element with many advantageous electrical, mechanical, and chemical properties.[19] In single-crystalline

GaN thin films, naturally formed permanent electric dipoles are already aligned in one direction, hence, electrical poling process is not required to obtain piezoelectric property, which is different from PZT.[19a,20] GaN is chemically and thermally stable and safe on human skin and in the body. It is stable and does not react with skin and body fluid.[21] The biocompatibility of GaN makes it a prime candidate to overcome the critical limitation of PZT in epidermic and implantable sensors and electronics.[19,20,22] Moreover, GaN thin films on flexible substrates showed excellent mechanical bendability and durability without degradation in materials and output characteristics of the devices, which provides an important benefit for reliable and continuous monitoring of the sensor. This characteristic is somewhat surprising considering the brittle nature of its bulk material; however, the durability and bendability of the film have been experimentally confirmed.[20b] Most importantly, GaN has a relatively high electromechanical coupling coefficient due to its low dielectric constant.[19a,20b] Single-crystalline GaN thin films were reported to show high performance in pressure sensing (output value, sensitivity, response time, and stability).[19b] Thus, GaN-based F-PEMS is the best option for the skin-attachable eye-movement detection application. In the present study, we investigate the operating principles and characteristics of the sensor for eye blinking and eyeball motions. The output signals generated by the sensor due to eye motion are numerically estimated, experimentally measured, and analyzed at various positions (upper eyelid, lower eyelid, and temple). As a result, we demonstrate for the first time that the eye movement sensor attached on a temple area of the face is capable to accurately measure various movements of eyes for noninvasive and reliable sensing in many extended applications.

## 2. Results and Discussion

### 2.1. Sensor Design and Fabrication

**Figure 1**a schematically illustrates the steps of the fabrication process of an F-PEMS. An edge area of the III-N thin films within ≈1 mm from the edges that was damaged during the dicing process was removed. Microcracks existing in the edge area could be propagated by mechanical stresses during the handling, attachment, and operation of the sensor, potentially resulting in the degradation of sensor performance. We can achieve the enhanced reliability and durability of the sensor by this process step. Optical microscope images of as-diced and edge-removed samples of GaN on Si confirm that microcracks in the edges within several hundred micrometers no longer exist after the edge removal (Figure S1, Supporting Information). Then, an electrode consisting of a stack of nickel, gold, copper, and gold (Ni/Au/Cu/Au) metal layers was deposited on top of the III-N thin-film surface, which will become a bottom electrode after the flip of the sample for further fabrication. A sapphire substrate was bonded to the electrode of the sample and the Si substrate was etched. Then, the sapphire was detached from the sample. After removing the Si and sapphire substrates, the sample was flipped and a top electrode with Ni/Au was deposited to complete the fabrication of the sensor element. Finally, the device was sealed by polydimethylsiloxane (PDMS) with wires attached to the electrodes. The top and bottom electrodes become anode and cathode, respectively. Detailed procedures are described in the Experimental Section.

Figure 1b shows a schematic structure of the fabricated F-PEMS having a flexible single-crystalline III-N film sandwiched between the electrodes. The F-PEMS is conformal for
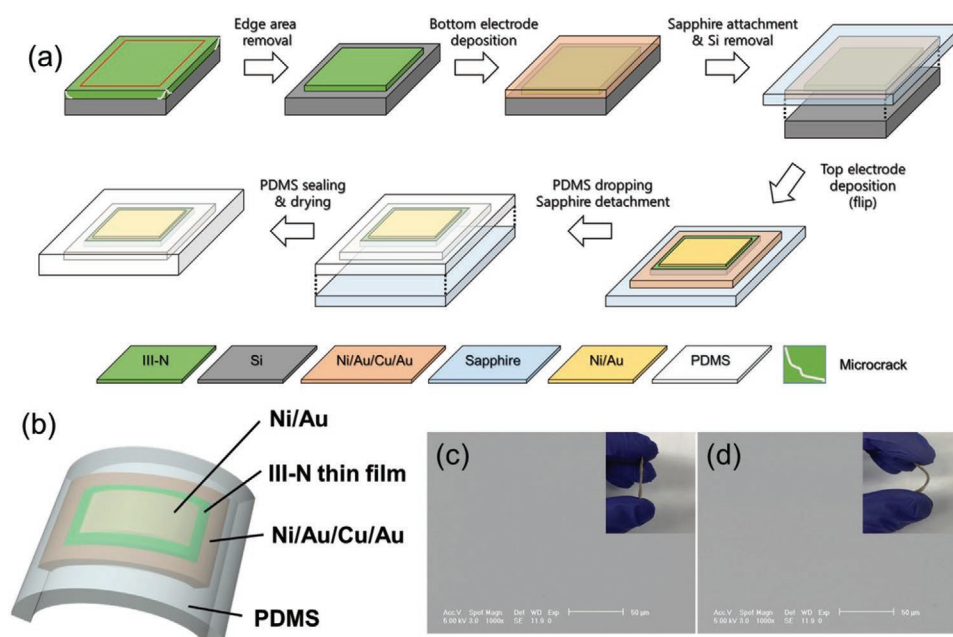


**Figure 1.** III-N thin-film-based flexible piezoelectric eye-movement sensor (F-PEMS). Schematic illustrations of a) the fabrication process steps and b) the structure. Scanning-electron microscopy (SEM) images of III-N thin-film surfaces with c) flat and d) bending test conditions. The insets of c) and d) show the bendability of the F-PEMS.

ADVANCED
SCIENCE NEWS
www.advancedsciencenews.com

ADVANCED
FUNCTIONAL
MATERIALS
www.afm-journal.de

the attachment of any skin surface and small enough for minimally invasive sensing. Furthermore, the output signal of the well-designed flexible piezoelectric sensor is higher than that of a rigid sensor with uniform deformation.[19b] Figure 1c,d shows the surface of a GaN film with flat and bending test conditions measured by scanning-electron microscopy (SEM) with similar bending conditions shown in the insets (bending angles of ≈0° and ≈90°). The F-PEMS surfaces are the same crack-free without surface features regardless of bending conditions, confirming that no bulk defect is generated even with a significant degree of bending.

## 2.2. Characteristics of Piezoelectric Sensing Element

The crystalline orientation and quality of the piezoelectric sensing element were investigated by high-resolution X-ray diffraction (HR-XRD). The III-N film on the Si (111) substrate was epitaxially grown to produce the single-crystalline wurtzite structure with a surface of (0001) plane. A III-N film's out-of-plane growth direction is aligned in a [0001] direction of wurtzite structure, which is confirmed by the strong presence of (000*l*) peaks, such as (0002) and (0004) (Figure S2a, Supporting Information). Therefore, a $d_{33}$ piezoelectric structure is constructed, since the sensing element is sandwiched between two electrodes (Figure 1b). Very sharp (0002) peaks of the III-N layers for both rigid and flexible substrates indicate the high crystalline quality of the sensing element before and after the fabrication of the device (Figure S2b, Supporting Information). Moreover, no other peak of wurtzite GaN, $Al_xGa_{1-x}N$, and AlN is observed in the $2\theta$-$\omega$ scan of XRD (Figure S2a, Supporting Information). Six sharp peaks are located at every 60° in the rotational scans ($\varphi$ scan) around GaN {$10\bar{1}2$} planes (Figure S2c, Supporting Information), i.e., sixfold rotational symmetry of the hexagonal-lattice structure (wurtzite), indicating that all the grains perfectly aligned in both in-plane and out-of-plane directions. Such XRD results confirm the single-crystallinity of the III-N film. After the transfer process of the III-N film, the peaks are maintained, which indicates no structural changes (Figure S2b,c, Supporting Information).

For the single-crystalline thin films, the density of crystalline line defects can be estimated from the rocking curves ($\omega$ scans) of symmetric and asymmetric planes, as shown in **Figure 2**. The full-width at half-maximum values of the GaN (0002) and GaN ($10\bar{1}2$) peaks on Si are 336 and 828 arc-seconds (arc-sec.), respectively. The density of threading dislocations of the single-crystalline GaN film is calculated to be ≈$3.2 \times 10^9$ cm$^{-2}$ using a method by Kagner et al.[23] Such a low density of line defects in single-crystalline material where no grain boundary exists is important to reduce the leakage between the electrodes, hence, to enhance the sensitivity of the sensor. The peaks in the rocking curves of the flexible substrate are broader than those of the Si substrate. This phenomenon is attributed to the wavy or curved nature of the sample rather than the degradation of crystalline quality itself. The intensities of GaN peaks on a flexible substrate, i.e., after the fabrication are lower than those on Si substrate, possibly due to the buried location of GaN under a top electrode.
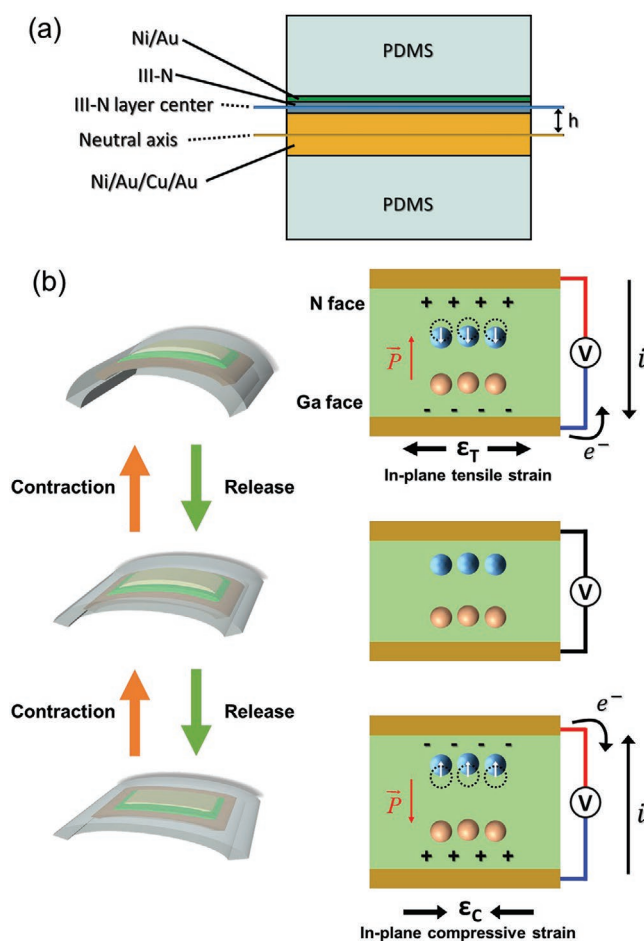
## 2.3. Sensing Mechanism of Eye Movements

The sensor is attached on a curved part of the skin near the eyes. After the attachment, the sensor is initially slightly bent depending on the contour of the skin of a face (**Figure 3**b middle). When the bending degree of the sensor is changed by the movement of the skin or muscles underneath, the change in piezoelectric polarization of the III-N film occurs. Because the bottom electrode is significantly thicker than the III-N film, a neutral plane of the F-PEMS is located in the Cu layer of the electrode (Figure 3a). This configuration induces only one type of piezoelectric polarization change (positive or negative) depending on the bending mode. When the sensor is further bent, in-plane tensile strain is applied and an upward piezoelectric polarization is accordingly induced. As a result, positive and negative charges are induced on the top (N-face) and bottom (Ga-face) surfaces, respectively. The electrical current flows from top to bottom electrodes through the external wires because of the free electron movement to cancel out the piezoelectric charges on the surfaces of GaN (Figure 3b top). Thus, the positive voltage output is measured. When the sensor is
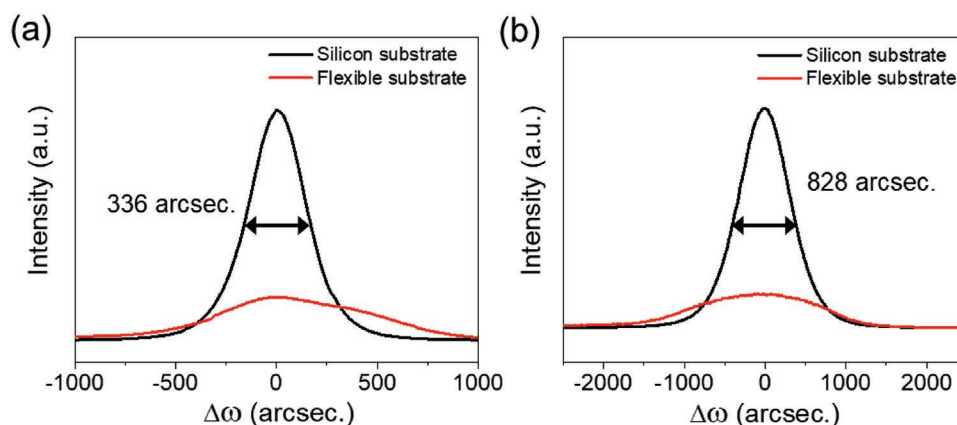


**Figure 2.** X-ray diffraction (XRD) characterization of the single-crystalline III-N thin film on rigid Si (black) and flexible Cu/PDMS (red) substrates. Rocking curves of a) GaN (0002) plane and b) GaN ($10\bar{1}2$) plane, indicating minimum spread in the out-of-plane and in-plane tilt of the single crystal.

**ADVANCED
SCIENCE NEWS**
www.advancedsciencenews.com

**ADVANCED
FUNCTIONAL
MATERIALS**
www.afm-journal.de

**Figure 3.** Voltage output change from the flexible piezoelectric eye sensor (F-PEMS) by piezoelectric polarization change with different bending modes of III-N film (N-faced). a) Cross-sectional structure of the F-PEMS showing a neutral plan located in Cu of the bottom electrode. When the sensor is further bent, more in-plane tensile strain is applied in the III-N film. When the sensor is flattened, less tensile (or more compressive from an initial bending state) in-plane strain is applied. b) Strain status, piezoelectric polarization change, and electric fields of the F-PEMS with an initial state (middle), further bending by the change in skin contour (top), and flattening by an opposite change in skin contour (bottom).

flattened, an in-plane compressive strain is applied and the negative voltage is measured (Figure 3b bottom). Further bending and flattening result in opposite signs in the output voltage of the F-PEMS.[19a] The change in skin contour by the eye movement is subtle; therefore, the sensor should be very sensitive to generate a substantial magnitude of the signal output voltage. We used COMSOL and MATLAB software to theoretically predict the output. Several parameters were applied including elastic modulus, Poisson ratio, unit weight, the thickness of film, sensor dimension (x and y), and applied load. **Figure 4**a shows the numerically simulated deflection and corresponding output voltages of the F-PEMS, confirming that the sensor is sensitive enough to measure the subtle contour change.

As described in the Introduction, accurate and reliable sensing of eye movement in a noninvasive and most comfortable way is important, therefore, the sensing on a temple area over upper and lower eyelid areas is preferred. While the

strain change on the skin of upper and lower eyelids is relatively straightforward, the skin contour change of the temple area is associated with muscle movement. The sensing mechanism of the F-PEMS on the temple is schematically illustrated in Figure 4. The bending status of the F-PEMS for contraction and release modes is shown in Figure 4b. As shown in Figure 4c,d, the sensor can be further bent or flattened from the initial condition (blue-dotted rectangle) by the eye blinking or eyeball motion by contraction and release force from muscle movement.[24] Therefore, the modes of eye movements generate different output voltages, i.e., opposite signs and varied magnitude. For the eye blinking, the main protractor of the eyelid, which serves to close the eye, is the orbicularis oculi and it is connected to the temple via ligament (Figure S3a, Supporting Information).[25] The ligament underneath of the temple is tightened or loosened for opening or closing of the eyelid during the eye-blinking process, respectively. For the eyeball movements, different muscles are involved (Figure S3, Supporting Information). Among these muscles, lateral rectus and medial rectus are principal parts for side-glance of the eyeball, which can be displayed with simulated results (lateral view) (Figure S4, Supporting Information).[24a] The muscles and ligament underneath the temple area are contracted when the eyeball moves toward the temple side (right) and are expanded when the eyeball moves away from the temple side (left).

### 2.4. Eye-Blink Sensing

**Figure 5** shows sensing characteristics for eye-blink movements, indicating that the F-PEMS yields substantial output voltage changes with various blink behaviors. Figure 5a shows three locations around the eye including images of a volunteer wearing the F-PEMS on the upper eyelid, lower eyelid, and temple using a biocompatible tape. This adhesive material is generally used and is strong enough to bond on human skin with high flexibility. It should be noted that the size of the sensor ($1 \times 1$ cm$^2$) is determined by the dicing size of the GaN/Si sample (Refer to the Experimental Section). The sensor can be made significantly smaller without affecting the output voltage signal that is not the function of the lateral dimension of the sensors. We experimentally confirm that the voltage output from sensors with different sizes including 0.25 cm$^2$ ($0.5 \times 0.5$ cm$^2$) and 4 cm$^2$ ($2 \times 2$ cm$^2$) are similar to those of the sensor used in this study.

The output voltages with eyelid movements as a function of measuring time are shown in Figure 5b–d from the F-PEMS attached on the upper eyelid, lower eyelid, and temple areas, respectively. The overall average values of output voltages are 97.85 and −96.02 mV for closing and opening on the upper eyelid, 78.31 and −79.42 mV for closing and opening on the lower eyelid, and 32.3 and −30.3 mV for closing and opening on the temple. The absolute values in the change are highest for the upper eyelid and lowest for the temple, which is related to the difference in the crooked level of the face parts. It is not surprising that the previous studies only show measurements from the eyelid area, which causes discomfort while wearing for the measurements. In this study, we demonstrate the measurement from the temple area. Signal-to-noise ratios (SNR,
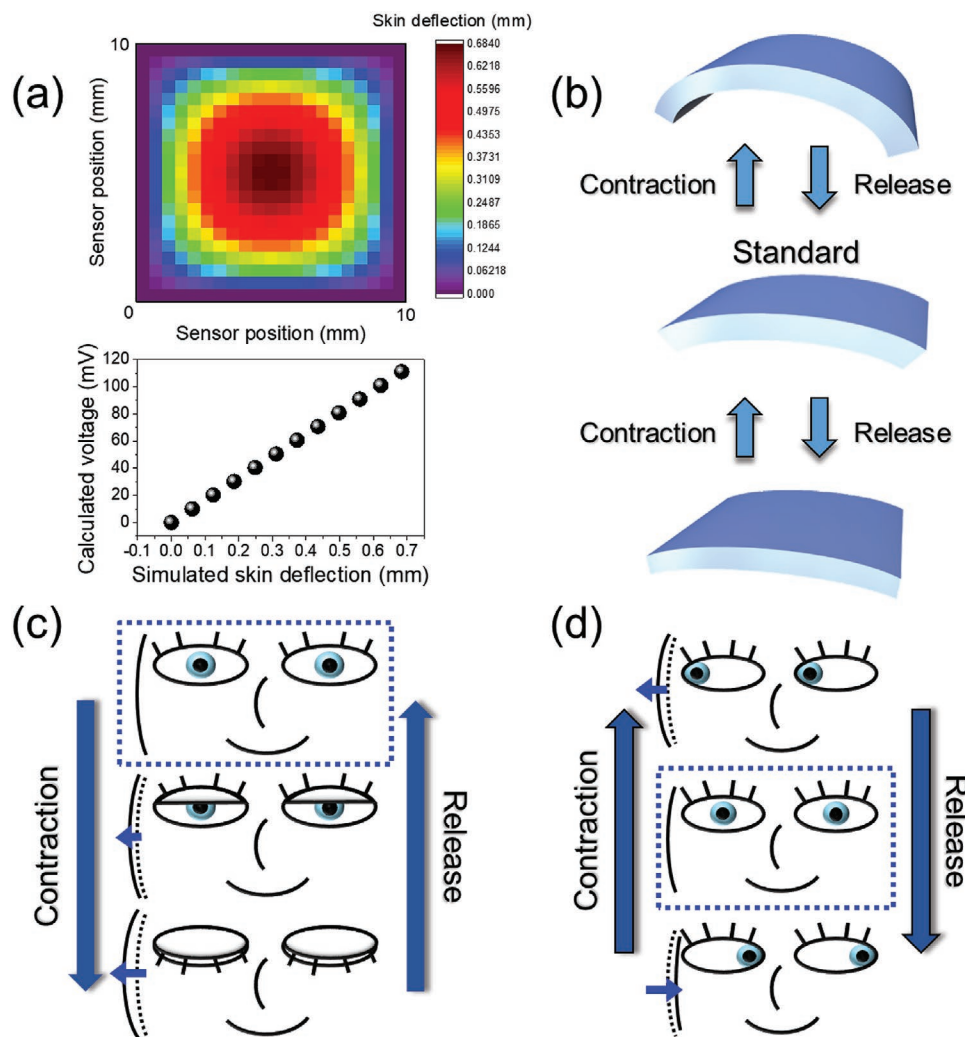
**Figure 4.** Sensing mechanisms of F-PEMS for eye blinking and eyeball movement. Numerical simulation of a) deflection of the sensor and generated voltage by skin contour change. Schematic illustration of b) bending motion of the F-PEMS as contraction and release, c) eye blinking and corresponding change in sensor deflection, and d) eyeball movement and corresponding changes in sensor deflection.

S/R) are 49.26 dB, 47.88 dB, and 40.13 dB for the measurements on the upper eyelid, low eyelid, and temple, respectively (Figure S5a, Supporting Information), calculated using the following equation
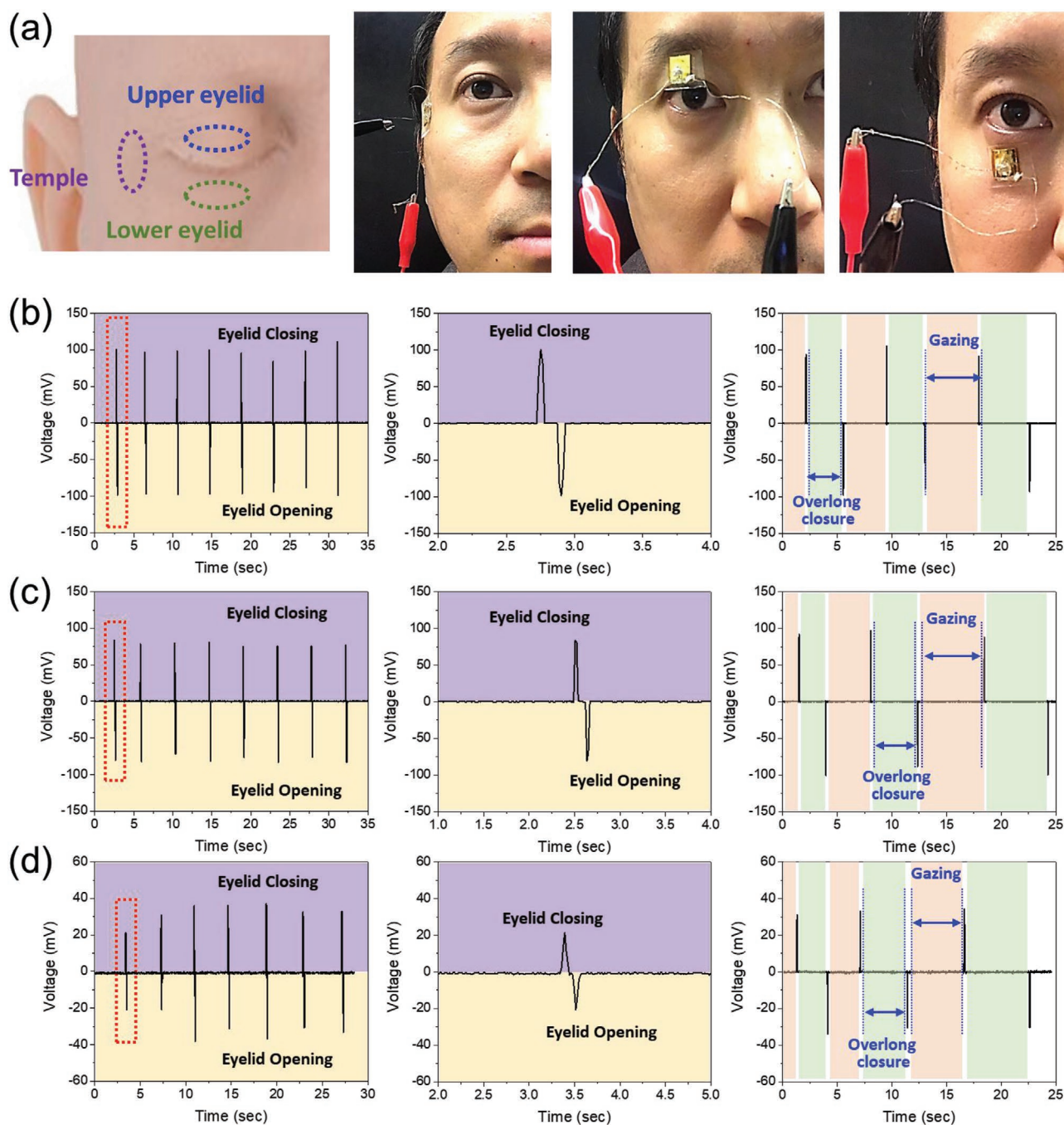
$$\text{SNR}_{dB} = 20 \log \left( \frac{V_{\text{signal}}}{V_{\text{noise}}} \right) \quad (1)$$

where $V_{\text{signal}}$ is the average value of output voltages and $V_{\text{noise}}$ is the averaged background signals. All the SNR values are greater than 40 dB, suggesting that the voltage values from the sensor on the temple are enough to communicate in wireless data.

Center figures of Figure 5b–d provide magnified output voltage curves from red-dotted rectangles in the left figures. They generate the positive and negative voltage outputs for the eyelid closing and opening, respectively, enabling to distinguish four stages of a normal eye blink motion, i.e., closing, closure, opening, and gazing (Figure S5b, Supporting Information). The eye closing corresponds to the output positively rising from zero to the peak. The output drops to and remains at zero until the further movement of the eyelid, corresponding to eye closure. The output changes in the opposite direction with increasing magnitude during the eye-opening, i.e., moving from zero to the valley. The output changes to and remains at zero during the gazing stage. The rapid eye blinking was also measured with higher frequency (0.24 → 1.67 Hz) (Figure S5c, Supporting Information). The flickering rate is influenced by short-term changes in the brain, such as tiredness and/or sleepiness.[1a] The voltage values are very similar to the outputs of blinking at a normal rate. These results indicate that the F-PEMS can be utilized to detect various eyelid movements for the evaluation of normal blinking, dry eyes, and drowsiness.

Long-term stability is one of the key parameters for the operation of sensors. The sensor on the skin was tested by continuous monitoring of eye blinking for 10 min followed by regular measurement every 30 min for ≈10 h. During the test, the human subject wore the sensor during the daily routine

ADVANCED
SCIENCE NEWS
www.advancedsciencenews.com

ADVANCED
FUNCTIONAL
MATERIALS
www.afm-journal.de

**Figure 5.** Sensing of eye blinking. a) Images of a face of a right showing 3 sensing locations (upper eyelid, lower eyelid, and temple) for eye movement measurement. Voltage output characteristics of sensing from b) upper eyelid, c) lower eyelid, and d) temple. Left figures of b–d) show overall sensing characteristics. Middle figures of b–d) show magnified outputs of the red-dotted rectangles in left figures. Right figures of b–d) show eyelid motion including overlong closure and overlong gazing instead of eye blinking.

without discomfort thanks to the conformal, compact, and noninvasive nature of the sensor. No degradation of the voltage output was observed for both the continuous monitoring and long-term monitoring (Figure S6, Supporting Information). No performance issue is expected for long-term continuous monitoring. The sensor can be reused by the subject in the following days. The stability and durability of the sensor are confirmed.

## 2.5. Fatigue and Drowsiness Detection

The degree of fatigue and drowsiness can be estimated by blink frequency, blink duration (delays of eye reopening), and PERCLOS (percentage of eye closure). A lid closure that lasts more than about 500 ms and covers the pupil for that time is usually defined as a microsleep. To simulate the state of the microsleep, overlong closure was investigated using the same

**ADVANCED
SCIENCE NEWS**

www.advancedsciencenews.com

**ADVANCED
FUNCTIONAL
MATERIALS**

www.afm-journal.de

positions. The overlong closure is of great interest in assessing workers, warfighters, and driving safety to detect blind working, blind walking, and drowsy driving, respectively. Right figures of Figure 5b–d show that the F-PEMS are capable to detect the microsleep in real-time. As marked in the figures, the sections of overlong closure and gazing are distinguished by the voltages upon the initiation of eyelid movement. For example, the gap between the positive and negative potentials is "overlong closure," whereas the interval between the negative and positive outputs is "gazing." Unlike the computer-vision-based ETS, the detection does not require additional calibration. The F-PEMS can directly provide the duration time for the overlong closure from the output change. Also, the response time of the F-PEMS is short enough to distinguish the four stages of eye blinking.

When people feel tired, they can be recognized through their eye changes, especially the blink of eyes, most quickly, as mentioned earlier. Also, when people are exhausted, their eyes are closing unconsciously while walking and driving.[1a] To investigate the fatigued eye, we simulated the status of dozing off and the volunteer closed his eyes half (here, almost half and 75% closed) and normal eye blink and half-blink were conducted alternately. Photographs of open eyes, half-closed eyes, and fully-closed eyes are shown in **Figure 6**a with the sensor on the temple. As mentioned above, eye blinking was approximately controlled as 50% and 75% level of normal blinking, the results of output voltages were plotted in Figure 6b, for 50% closed and 75% closed, respectively, between voltages from normal blinking. The outputs are relatively small value (≈50% for half-closing and 72% for 75% closing), which means that we can discern the condition of the eye from output voltages. The results from other parts (upper eyelid and lower eyelid) with the half-closed condition show a similar tendency to the

output voltages from the temple area (Figure S7, Supporting Information).
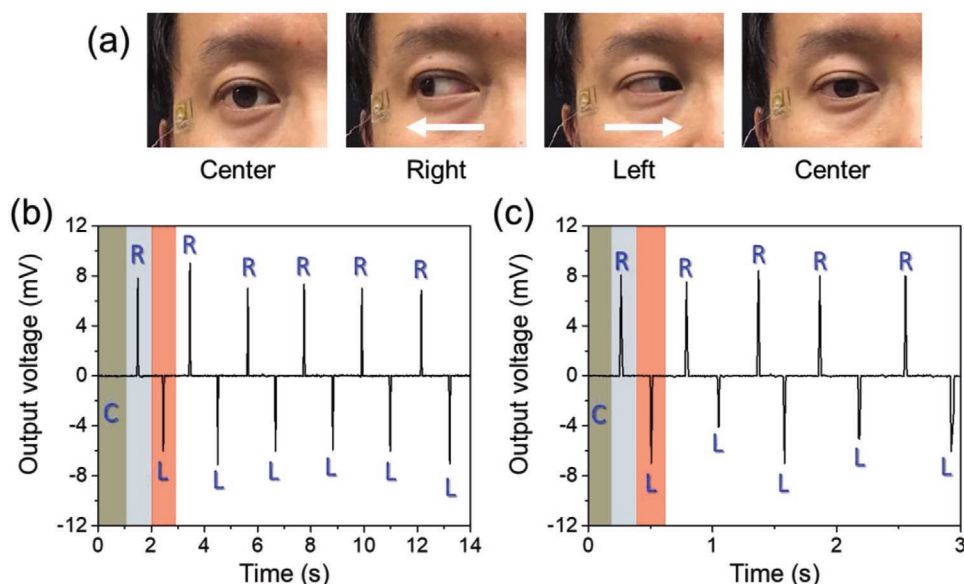
## 2.6. Eyeball-Movement Sensing

In addition to the sensing of eye blink for the detection of eye fatigue and drowsiness, the F-PEMS can measure the movement of the eyeball, which is related to sleeping patterns, the additional diagnosis of brain-related diseases, and eye tracking in AR/VR systems. **Figure 7** shows the output characteristics of the sensor attached on the right-side temple of the face when the eyeball moves in a lateral direction. When the eyeball moves to the right, i.e., moving toward the sensor side, positive values are measured. In contrast, when the eyeball moves in the opposite direction, i.e., moving away from the sensor side, negative values are obtained. This output is different from the signal of the EOG that measures the potential difference between cornea and retina, which is influenced by numerous external conditions, e.g., light intensity, number of electrodes, skin status, and noise from contact resistance. As the contraction of the lateral rectus pulls the eye away from the nose (right seeing), the sensor is further bent (Figure S4, Supporting Information). Conversely, as the contraction of the medial rectus pulls the eye toward the nose (left seeing), the sensor is flattened (Figure S4, Supporting Information).[24a,25] The eyeball moving to the right and the left sides corresponds to contraction and release of the F-PEMS, respectively (Figure 4d). When the eyeball moves toward the sensor side, further bending of the sensor occurs, hence positive voltage output is generated. When the eyeball moves away from the sensor side, the negative voltage output is generated. The output characteristics were
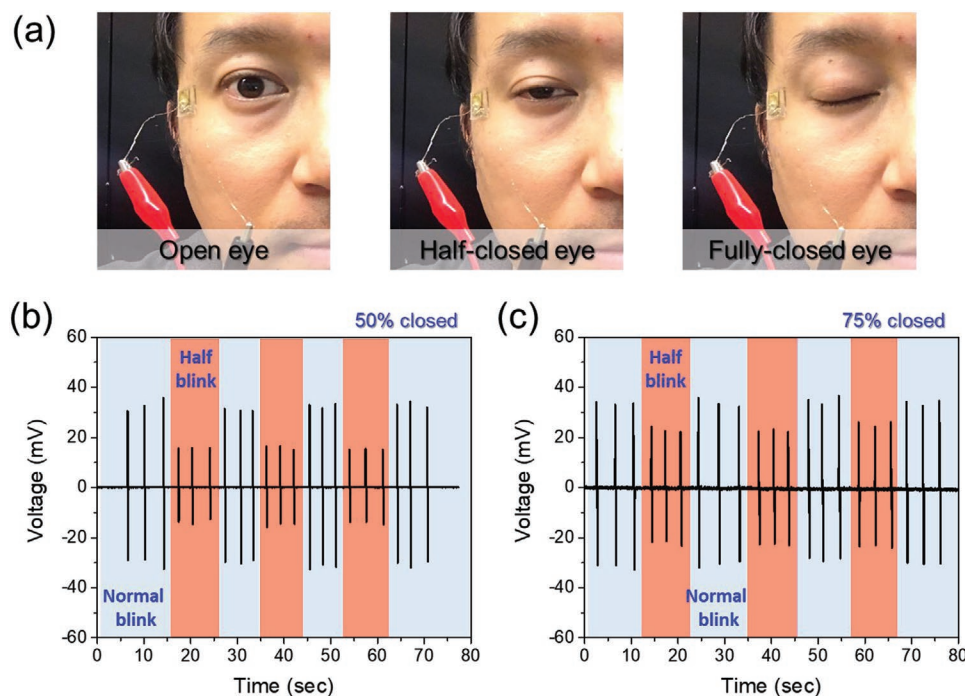


**Figure 6.** Detection of generated voltages from half-blinking for mimicking of fatigue eye. a) Photographs of open, half-closed, fully closed eye. Voltages from normal blinking and b) 50% closed eye and c) 75% closed eye.

**Figure 7.** Sensing of eyeball movement. a) Photographs of eyeball motion from the center (C)—right (R)—left (L)—center (C) with F-PEMS attached on the temple. Output voltages measured by b) slow and c) rapid eyeball motion.

measured in both cases of slow (≈0.5 Hz) and rapid (≈1.9 Hz) eye movement, as shown in Figure 7b,c, respectively, showing similar output voltage values regardless of the speed of the motion. In Figure 7c, the initiation of the lateral eye movement can be detected with a fast response time. The output from different sensor positions (upper eyelid and lower eyelid) shows a similar trend only with higher output voltage values, attributed to relatively larger deformation of the F-PEMS (Figure S8, Supporting Information). The overall values of voltage output are different for eyelid movements (≈30 mV) and eyeball movements (≈10 mV). Therefore, each movement is distinguishable for the sensing of combined movements of eye blinking and eyeball moving. Moreover, further detailed movement of eyeballs (vertical and oblique directions and rotational movements) and eyelid (left and right separately) could be detected if arrayed (e.g., 1 × 3) sensors are attached on both sides of the temples.

## 3. Conclusion

A F-PEMS was designed, fabricated, and tested to develop a personal safety, behavior, and healthcare monitoring sensing network. A stable and safe piezoelectric single-crystalline III-N thin film was epitaxially grown on a Si (111) substrate and then transferred to a flexible PDMS substrate followed by the electrode formation. The fabricated F-PEMS was tested on several different parts around the eyes, including the upper eyelid, lower eyelid, and temple area. The sensor was estimated to generate substantial output voltage signals enough to detect small deflections of muscles and skins caused by eyelid and eyeball movements based on numerical simulation and demonstrated to measure normal eye blinking with signal-to-noise ratios of higher than 40 dB, confirming high sensitivity and usability for wireless communication systems. Especially, the sensor was capable to detect various movements of eyelid and eyeballs

from the most-comfortably-wearable temple area. This non-invasive, nontoxic, and easily-wearable eye movement sensor can detect eye blink frequency, blink duration, and percent of eye closure to function as an objective indicator of eye strain, fatigue, and drowsiness. The sensor can also measure lateral movements of eyeballs, which are distinguished from the eye blink, for the potential use of medical diagnosis indicators of autism, ADHD, stroke, Alzheimer and Parkinson's disease as well as in industrial applications such as VR and AR in remote control of robots.

## 4. Experimental Section

*Single-Crystalline III-N Thin Film Growth*: For the synthesis of the single-crystalline GaN thin film without impurities, III-N layers were epitaxially grown by metalorganic chemical vapor deposition (MOCVD) on a (111) Si substrate using trimethylaluminum (TMAl, Al(CH₃)₃), trimethylgallium (TMGa, Ga(CH₃)₃), and ammonia (NH₃) gases as precursors and hydrogen (H₂) as a carrier gas. An aluminum nitride (AlN) buffer layer was first grown on the Si substrate with a thickness of ≈100 nm and there is no interaction between AlN and Si not to form a secondary phase. Then, step-graded aluminum gallium nitride (Al$_x$Ga$_{1-x}$N) layers were grown with increasing GaN mole fractions for a total thickness of ≈600 nm. Finally, an ≈2 μm thick unintentionally-doped GaN layer was grown at 1050 °C and 200 Torr. Cracks or other structural defects were not observed in the epitaxial thin films after the cool-down.

*Dicing and Removal of Fine Cracks from Edge Area of Small Samples*: The epitaxial wafer was cut into pieces of samples by dicing, e.g., 1 × 1 cm². The sample was cleaned in an ultrasonicator with acetone for 1 min, then rinsed with isopropyl alcohol and deionized (DI) water followed by nitrogen (N₂) gas blowing for drying. The samples usually contain fine cracks near the edges, damage associated with the dicing process. For the removal of the cracks, a selected area of the III-N thin film was patterned by photolithography. A photoresist (PR, MicroChemicals, AZ4620) was spin-coated at 3000 rpm for 60 s, then baked on a hot plate at 110 °C for 180 s. The PR was exposed by mask aligner (ABM, TTMA)

ADVANCED
SCIENCE NEWS

www.advancedsciencenews.com

ADVANCED
FUNCTIONAL
MATERIALS

www.afm-journal.de

with 365 nm ultraviolet ray and a dose of 500 mJ cm$^{-2}$ and developed in a developer (MicroChemicals, AZ400K with DI water, 1:2 volume ratio) for 40 s to expose the edge area with fine cracks. A deep reactive-ion etching (Oxford Plasmalab System 100/ICP180) was applied to remove the damaged III-N layers with argon (Ar) and chlorine (Cl$_2$) gas. After the plasma etching, the PR was removed by acetone.

*Bottom Electrode Deposition*: A bottom electrode, Ni/Au/Cu/Au, was formed on the top surface of the GaN layer. Ni (≈5 nm) and Au (≈100 nm) layers were deposited by electron beam (E-beam) evaporation (Thermionics). Then, for mechanical support, a Cu layer (≈10 μm) was deposited by electroplating with 0.1 M of CuSO$_4$ solution as an electrolyte at a current density of 0.1 A cm$^{-2}$. Finally, an Au layer (≈100 nm) was coated by a desktop sputtering system (Denton Desk II).

*Removal of Si Substrate*: Before the substrate removal, a sapphire substrate was attached on the top side of the sample with polymeric rosin by a hot plate at 120 °C. Then, Si substrate was removed by a wet etching process using a mixed acidic solution, hydrofluoric acid (HF, 49%, Macron fine chemicals), acetic acid (CH$_3$COOH, 50%, Macron fine chemicals), and nitric acid (HNO$_3$, 70%, Fisher chemical) with a volume ratio of 80:15:5, respectively.

*Top Electrode Deposition*: A top electrode, Ni/Au, was formed on the bottom surface of the AlN layer where the Si substrate was removed. Ni (5 nm) and Au (100 nm) layers were deposited by E-beam evaporation.

*PDMS Coating for Sealing*: Liquid PDMS (Dow Corning Sylgard 184) consisting of a base and a curing agent with a 10:1 weight ratio and the mixed suspension was dropped to the fabricated sensor. Opening areas were also created for connecting the leading wire to the electrodes. Then, the packaged sensor was heated in an electrical oven at 90 °C for 3 h for curing. The biocompatible tape (3M clear medical tape roll, double-sided) was used for the attachment of the sensor to the volunteer's skin.

*Characterization and Measurements*: The III-N thin films were characterized by HR-XRD, (Bruker D8 Discover) to investigate their crystalline structure and crystallinity. The surface was observed by SEM (FEI XL-30FEG) and optical microscope (Keyence VHX-600) to examine the existence of cracks and surface conditions. A programmable electrometer (Keithley 6514) was used to measure the output voltages of the sensor at different sites as eyes blink and eyeballs move. Real-time data acquisition was conducted by LabVIEW-based software connected to the electrometer with a data-acquisition board (National Instrument USB-6212 BNC). The IRB reviewed the scope of the research and determined that formal approval is not required. The volunteer agreed to participate in this study with informed consent.

## Supporting Information

Supporting Information is available from the Wiley Online Library or from the author.

## Conflict of Interest

The authors declare no conflict of interest.

[1]  a) S. Benedetto, M. Pedrotti, L. Minin, T. Baccino, A. Re, R. Montanari, *Transport. Res. Part F: Traffic Psychol. Behav.* **2011**, *14*, 199; b) K. Saito, *Ind. Health* **1999**, *37*, 134.

[2]  B. C. Tefft, *Accid. Anal. Prev.* **2012**, *45*, 180.

[3]  J. S. Higgins, J. Michael, R. Austin, T. Åkerstedt, H. P. A. Van Dongen, N. Watson, C. Czeisler, A. I. Pack, M. R. Rosekind, *Sleep* **2017**, *40*, zsx001.

[4]  W. W. Wierwille, L. A. Ellsworth, *Accid. Anal. Prev.* **1994**, *26*, 571.

[5]  J. Vicente, P. Laguna, A. Bartra, R. Bailón, *Med. Biol. Eng. Comput.* **2016**, *54*, 927.

[6]  C. Jacobé de Naurois, C. Bourdin, A. Stratulat, E. Diaz, J.-L. Vercher, *Accid. Anal. Prev.* **2019**, *126*, 95.

[7]  E. Wilkinson Vanessa, L. Jackson Melinda, J. Westlake, B. Stevens, M. Barnes, P. Swann, M. W. Rajaratnam Shantha, E. Howard Mark, *J. Clin. Sleep Med.* **2013**, *09*, 1315.

[8]  K. Koch, J. McLean, R. Segev, M. A. Freed, M. J. Berry, V. Balasubramanian, P. Sterling, *Curr. Biol.* **2006**, *16*, 1428.

[9]  a) Y. Groen, N. A. Börger, J. Koerts, J. Thome, O. Tucha, *J. Neural Transm.* **2017**, *124*, 27; b) S.-H. Kim, J.-S. Kim, *Acta Neurol. Belg.* **2019**, *119*, 37; c) M. Micai, H. Joseph, M. Vulchanova, D. Saldaña, *Autism Res.* **2017**, *10*, 888; d) V. Biousse, B. C. Skibell, R. L. Watts, D. N. Loupe, C. Drews-Botsch, N. J. Newman, *Neurology* **2004**, *62*, 177; e) M. L. F. Pereira, M. v. Z. A. Camargo, I. Aprahamian, O. V. Forlenza, *Neuropsychiatr. Dis. Treat.* **2014**, *10*, 1273.

[10]  a) B. N. Türkan, S. Amado, E. S. Ercan, I. Perçinel, *Res. Dev. Disabil.* **2016**, *49–50*, 205; b) T. W. Frazier, E. W. Klingemier, M. Beukemann, L. Speer, L. Markowitz, S. Parikh, S. Wexberg, K. Giuliano, E. Schulte, C. Delahunty, V. Ahuja, C. Eng, M. J. Manos, A. Y. Hardan, E. A. Youngstrom, M. S. Strauss, *J. Am. Acad. Child Adolesc. Psychiatry* **2016**, *55*, 301; c) E. Vakil, M. Mass, R. Schiff, *J. Atten. Disord.* **2016**, *23*, 1160.

[11]  L. M. Schmitt, E. H. Cook, J. A. Sweeney, M. W. Mosconi, *Mol. Autism* **2014**, *5*, 47.

[12]  a) E. Newman-Toker David, S. Saber Tehrani Ali, G. Mantokoudis, H. Pula John, I. Guede Cynthia, A. Kerber Kevin, A. Blitz, H. Ying Sarah, Y.-H. Hsieh, E. Rothman Richard, F. Hanley Daniel, S. Zee David, C. Kattah Jorge, *Stroke* **2013**, *44*, 1158; b) A. Pollock, C. Hazelton, C. A. Henderson, J. Angilley, B. Dhillon, P. Langhorne, K. Livingstone, F. A. Munro, H. Orr, F. J. Rowe, U. Shahani, *Cochrane Database Syst. Rev.* **2011**, *10*, CD008389.

[13]  K. A. Pelphrey, N. J. Sasson, J. S. Reznick, G. Paul, B. D. Goldman, J. Piven, *J. Autism. Dev. Disord.* **2002**, *32*, 249.

[14]  a) P. Maquet, J.-M. Péters, J. Aerts, G. Delfiore, C. Degueldre, A. Luxen, G. Franck, *Nature* **1996**, *383*, 163; b) E. Aserinsky, N. Kleitman, *Science* **1953**, *118*, 273.

[15]  a) T. Koike, S. Kan, M. Misaki, S. Miyauchi, *Neurosci. Res.* **2011**, *69*, 322; b) M. C. Dumoulin Bridi, S. J. Aton, J. Seibt, L. Renouard, T. Coleman, M. G. Frank, *Sci. Adv.* **2015**, *1*, e1500105.

[16]  a) J. Iskander, M. Hossny, S. Nahavandi, *Appl. Ergon.* **2019**, *81*, 102883; b) A. Szpak, S. C. Michalski, D. Saredakis, C. S. Chen, T. Loetscher, *IEEE Access* **2019**, *7*, 130883.

[17]  a) Z. Ye, Y. Li, A. Fathi, Y. Han, A. Rozga, G. D. Abowd, J. M. Rehg, in *Proceedings of the 2012 ACM Conference on Ubiquitous Computing*, Association for Computing Machinery, Pittsburgh, PA **2012**,

p. 699; b) A. Bulling, H. Gellersen, *IEEE Pervasive Comput.* **2010**, *9*, 8; c) D. Zoccolan, B. Graham, D. Cox, *Front. Neurosci.* **2010**, *4*, 193.

[18] a) S. Lee, R. Hinchet, Y. Lee, Y. Yang, Z.-H. Lin, G. Ardila, L. Montès, M. Mouis, Z. L. Wang, *Adv. Funct. Mater.* **2014**, *24*, 1163; b) C. Lü, S. Wu, B. Lu, Y. Zhang, Y. Du, X. Feng, *J. Micromech. Microeng.* **2018**, *28*, 025010; c) X. Pu, H. Guo, J. Chen, X. Wang, Y. Xi, C. Hu, Z. L. Wang, *Sci. Adv.* **2017**, *3*, e1700694; d) S. Lee, S.-H. Bae, L. Lin, Y. Yang, C. Park, S.-W. Kim, S. N. Cha, H. Kim, Y. J. Park, Z. L. Wang, *Adv. Funct. Mater.* **2013**, *23*, 2445.

[19] a) J. Chen, H. Liu, W. Wang, N. Nabulsi, W. Zhao, J. Y. Kim, M.-K. Kwon, J.-H. Ryou, *Adv. Funct. Mater.* **2019**, *29*, 1903162; b) N.-I. Kim, Y.-L. Chang, J. Chen, T. Barbee, W. Wang, J.-Y. Kim, M.-K. Kwon, S. Shervin, M. Moradnia, S. Pouladi, D. Khatiwada, V. Selvamanickam, J.-H. Ryou, *Sens. Actuators, A* **2020**, *305*, 111940.

[20] a) J. Ryou, P. D. Yoder, J. Liu, Z. Lochner, H. Kim, S. Choi, H. J. Kim, R. D. Dupuis, *IEEE J. Sel. Top. Quantum Electron.* **2009**, *15*, 1080; b) J. Chen, S. K. Oh, N. Nabulsi, H. Johnson, W. Wang, J.-H. Ryou, *Nano Energy* **2019**, *57*, 670.

[21] S. A. Jewett, M. S. Makowski, B. Andrews, M. J. Manfra, A. Ivanisevic, *Acta Biomater.* **2012**, *8*, 728.

[22] J. Chen, S. K. Oh, H. Zou, S. Shervin, W. Wang, S. Pouladi, Y. Zi, Z. L. Wang, J.-H. Ryou, *ACS Appl. Mater. Interfaces* **2018**, *10*, 12839.

[23] V. M. Kaganer, O. Brandt, A. Trampert, K. H. Ploog, *Phys. Rev. B* **2005**, *72*, 045423.

[24] a) J. M. Miller, *Vision Res.* **1989**, *29*, 223; b) K. Schmidtke, J. A. BÜTtner-Ennever, *Brain* **1992**, *115*, 227.

[25] C. J. Moss, B. C. Mendelson, G. I. Taylor, *Plast. Reconstr. Surg.* **2000**, *105*, 1497.